Journal of *Marine Science and Engineering*

MDPI

Article

Study of the Hull Structural Deformation Calculation Using the Matrix Displacement Method and Its Influence on the Shaft Alignment

Weixin Zhou [1], Yao Zhao [1], Hua Yuan [1] and Xiaoqiang Wang [2,*]

[1] School of Naval Architecture and Ocean Engineering, Huazhong University of Science and Technology, Wuhan 430074, China
[2] School of Naval Architecture and Ocean Engineering, Naval University of Engineering, Wuhan 430033, China
* Correspondence: wxq_nue@126.com

Abstract: The analysis of the influence of hull deformation on shaft alignment is predominately conducted using the finite element method (FEM), which is time-consuming, labor-intensive, and challenging to use for iterative hull design optimization. In this paper, hull deformation is separated into two parts—global deformation and local deformation, simplified to a single-span beam model and a grillage beam model, respectively—then solved using the matrix displacement method (MDM). Compared to FEM, the proposed method has a small calculation error, proving its correctness, while the calculation time is greatly reduced. The proposed method has been used to calculate the hull deformation of a ship under various conditions and evaluate its influence on shaft alignment. The results indicate that under certain conditions, the bearing reaction forces are constant, whereas the bearing pressure changes as a consequence of the change in shaft-to-bearing angle. The comparison between local rotation and shaft-to-bearing angle reveals that bearings in various positions follow distinct laws. We suggest that the shaft-to-bearing angle be used as an additional parameter in the evaluation of shaft alignment calculations. Moreover, when optimizing bearing pressure, bearings in different positions are affected differently by global and local deformation, and their optimization priorities are distinct.

Keywords: hull deformation; global deformation; local deformation; shaft alignment; matrix displacement method; bearing pressure

Citation: Zhou, W.; Zhao, Y.; Yuan, H.; Wang, X. Study of the Hull Structural Deformation Calculation Using the Matrix Displacement Method and Its Influence on the Shaft Alignment. *J. Mar. Sci. Eng.* **2023**, *11*, 1495. https://doi.org/10.3390/jmse11081495

Academic Editor: Vincenzo Crupi

Received: 7 July 2023
Revised: 24 July 2023
Accepted: 26 July 2023
Published: 27 July 2023

1. Introduction

With increasing hull scale, hull deflection has a greater effect on shaft alignment. The use of high-strength steel and the tendency toward growing ship scale, on the one hand, increase the hull's flexibility, which, in turn, increases the change in shaft support displacement as a result of hull deformation [1,2]. A longer and larger shaft, on the other hand, results in a larger scale of bearings and a heavier load, increasing the thrust force to meet the power needs of larger ships. This raises two issues. The first is how to calculate the impact of ship deformation on shaft alignment. The second is whether the influence of the higher bearing scale can be captured by the bearing load alone.

For ship deformation calculations, the ship hulls are three-dimensional shell structures for which direct theoretic calculations are nearly impossible to perform [3]. In the past, the ship hull was simplified to a beam [4], and only the global deformation was considered. The disadvantage of this treatment is, on the one hand, low accuracy, as the deformation of the hull cross section [5] is disregarded. Additionally, it is detrimental to the optimal design of the hull structure. Regarding the effect of hull deformation on the shafting, the bearing support is only located at a specific location on the hull. The optimal design only requires reinforcement of the local structure near the bearing, but the calculation of the hull beam cannot account for the local structural changes.

With the development of computer technology, FEM has become a popular method in engineering [6]. Some researchers have utilized FEM to analyze the impact of hull deformation on shaft alignment [7–10]. The method divides the complex three-dimensional hull structure into discrete elements [11]. When the elements are of high quality, the results are accurate. Nevertheless, there are several drawbacks associated with utilizing FEM. First, hull structure modeling is time-consuming and labor-intensive. However, the actual required deformation value is limited to only a few specific points. Secondly, FEM calculation is a post-design evaluation method because the construction of the structure model in the FEM analysis requires precise information. In addition, the results of FEM are still unable to distinguish between global and local deformations. Although the results include the amount of local deformation, the effects of global deformation and local deformation on the shaft alignment remain unclear. When considering optimal design, a better structural form can only be found by the exhaustive method.

Some scholars have attempted to analyze the effect of hull deformation on shaft alignment using direct measurements. There are three main measurement methods. The first is the load method [12], which employs the jack-up method to measure the bearing load. In the second method, the wireless strain method, strain gauges are positioned on the shaft, and data are transmitted wirelessly [13,14]. The idea of this method is to calculate the bearing displacement by observing the variation in the shaft moment. The third technique is the laser measurement method [15,16], which gauges bearing offset using laser calibration. However, the measurement methods do have significant limitations, and they are not yet widely employed. The load method can only be employed statically, the strain measurement method cannot be employed for an extended period of time, and the laser measurement method requires an unhindered optical channel. Furthermore, none of the three methods can be used to measure bearings underwater.

For the second issue, there is an increasing number of cases of bearing damage leading to shaft failure as the bearing scale increases [17]. For example, three advanced offshore patrol vessels belonging to the Indian Coast Guard have found the same excessive bearing wear [18]; four of the six ships built by a Chinese shipyard suffered frequent bearing failure [19]; and 11 out of the 17 ships constructed in a single shipyard were subjected to issues related to bearing faults [15]. In the shaft alignment calculation, the bearing load, or mean pressure, is the sole parameter used to evaluate bearing failure [20–23]. However, it is unlikely that all bearings on the same type of ship are overloaded. As the scale of the entire shaft system increases, the distance between bearings increases, making individual bearings less sensitive to offset, whereas the increase in bearing size complicates the interaction between bearing and shaft. Therefore, additional quantities must be introduced to evaluate the impact of the alignment change on the bearing's operating condition. Analysis of the bearing failure form demonstrates that side abrasion with an angle between the shaft and the bearing also occurs frequently. An increasing amount of research [24–26] has discovered that the relative angle influences the load area and pressure distribution of a single bearing significantly. As the scale of the bearing increases, it becomes inappropriate to analyze the bearing's operating condition by simplifying the bearing to a simple point and ignoring the relative position relationship between the shaft and the bearing. Consequently, it is essential to consider the relative angle between the shaft and the bearing, which indicates the distribution of the loaded region of the bearing.

The contribution of this paper is that the hull deformation affecting shaft alignment is separated into two parts—global deformation and local deformation, simplified to a single-span beam model and a grillage beam model, respectively—then solved using the MDM. This is advantageous for optimizing the hull structure to alleviate the high bearing pressure caused by misalignment. On the one hand, the proposed method has a substantial labor and time consumption advantage over FEM. The proposed method can be modeled and solved within a few hours. In contrast, modeling and analyzing the structural deformation of an entire ship using FEM typically takes several weeks. Comparing the results of the two methods, however, reveals that the error introduced by the simplification in the proposed

method is minimal. The high efficiency and accuracy of the proposed method allow iterative optimization to be used in hull structure optimization. In addition, the proposed method makes it possible to evaluate the degree to which each bearing is influenced by the two components and to make targeted adjustments when optimizing. Particularly, bearings that are primarily affected by local deformations can achieve substantial pressure relief advances with very minor structural modifications.

This paper is organized as follows. Section 1 reviews the effect of hull deformation on shaft alignment. Section 2 describes the simplified modeling of the global and local hull deformations and the computation process using the MDM. Section 3 compares the proposed method with FEM to compute the deformation of a box beam model. Section 4 presents a case study using the proposed methodology to calculate the effect of global and local deformation on the bearing pressure of ships under different conditions. Section 5 concludes the study and provides suggestions for further work.

2. Hull Deformation Calculation Using the MDM

As one of a ship's many systems, the propulsion shaft system is borne in the hull structure, is affected by the deformation of the hull structure, and operates relatively independently. In this section, the main parameters of the hull deformation calculation are determined for the shaft alignment calculation based on the hull–bearing–shaft structure form. The global deformation and local deformation of the hull are then calculated according to the beam theory, and the combined results are used to analyze the influence of hull deformation on shaft alignment.

2.1. Hull–Bearing–Shaft Interaction Analysis

A schematic diagram of the hull–bearing–shaft coupling structure is shown in Figure 1. The propulsion shaft system is typically located at the stern end of the vessel bottom, beginning at the thrust bearing or main engine and terminating at the propeller. The rotating elements are unified into a shaft system, and ancillary structures such as couplings that rotate with the shaft system can be considered to be intrinsic to the shaft. The shaft system is only weakly constrained by the bearing. Comparing the length of the bearing to the length of the shaft reveals that the bearing can be simplified to a point restraint when analyzing the shaft deformation. The bearing constraints on the shaft system are reflected in both the vertical and lateral dimensions, but the lateral load is significantly less than the vertical load, so the vertical force is typically considered. Therefore, the function of the bearing in the shaft system can be reduced to a single-point force opposing gravity [27]. From the forces of the shaft system, it can be seen that the main loads are in the longitudinal plane, i.e., the OYZ plane, as shown in Figure 1.

Moreover, unless otherwise specified, the coordinate systems in this paper correspond to those in Figure 1, i.e., the ship's length is in the Z direction and is positive toward the bow. The direction of the ship's height is Y, and upward is positive. The breadth of the ship is measured in the X direction, which is positive toward the port side. The directions of positive displacement, rotation, force, and moment correspond to those specified for the coordinate system.

As depicted in Figure 2, the structure of the bearing is that of a sliding bearing, which consists of a bearing holder and a bearing bush. The holder is typically fixed directly to the hull, and its thickness is significantly greater than that of the hull shell, so its deformation is minimal. The bearing bush and the shaft journal constitute a friction pair. There is a small gap between them, which is filled with lubricant to reduce friction. The majority of bearing failure is caused by damage to the bush, which can be caused by a variety of factors, but its working condition can be determined by its internal pressure distribution. Both the contact pressure under the dry friction condition and the hydrodynamic pressure under the hydrodynamic lubrication condition can directly reflect the bearing's operating condition. This pressure parameter is influenced primarily by the relative position of the shaft journal and bearing bush. The bearing's upper and lower positions influence the magnitude of its

reaction force, while the fore and tail trim angles (rotation angles around the OX axis) and the left and right swing angles (rotation angles around the OY axis) of the bearing influence the internal pressure area and the distribution of pressure values. The research conducted by Zhang [28] demonstrates that the effect of the trim angle is significantly greater than that of the swing angle. Therefore, the parameters to be considered are the bearing's vertical position and the trim angle.

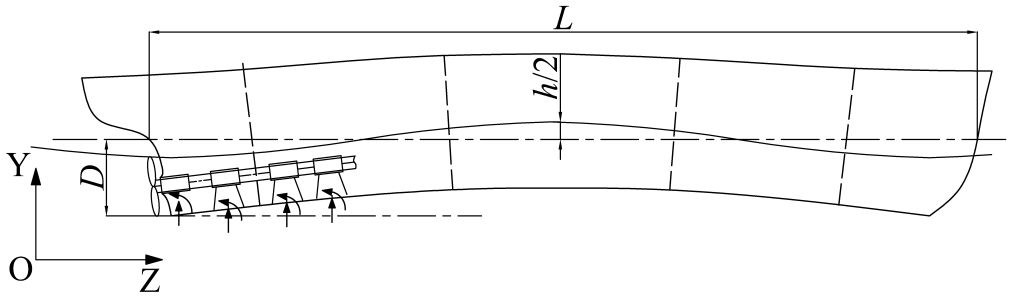

Figure 1. Schematic diagram of hull–bearing–shaft structure.

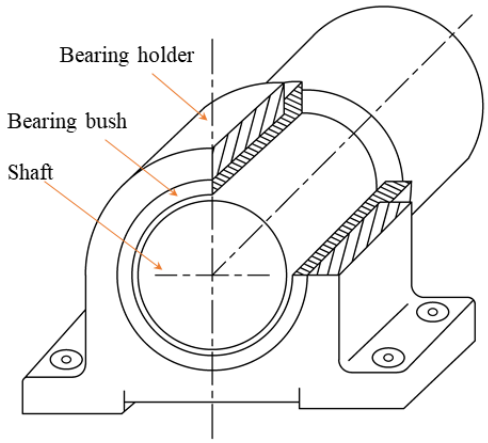

Figure 2. Schematic diagram of the bearing structure.

In terms of the hull structure, the hull is subject to the same gravitational force as the bearings due to the propulsion shaft. The change in reaction force resulting from a change in bearing position is negligible compared to the load that causes hull deformation. Therefore, the effect of the change in reaction force on global hull deformation is negligible, but it does have some effect on local plate deformation when the bearing offset is large. In addition, analysis of the shaft system and bearings from the front reveals that the vertical position and bearing trim angle (both in the OYZ plane) are the critical quantities for analysis of the shaft alignment. As a long, thin-walled beam structure, the ship is also primarily loaded by gravity and buoyancy, and longitudinal section deformation is still superior to other forms of deformation. Consequently, the analysis of hull deformation can also be focused on the OYZ plane.

2.2. The Global and Local Deformation Calculation Using the MDM

Ship deformation varies with internal and external loads, such as loading and waves, resulting in various offsets of bearings in different locations. Bearing offset consists of two components. First, global deformation is calculated by corresponding the hull to a non-uniform beam and ignoring the cross-sectional deformation, assuming that the deformation at each point of the cross section is the same as the neutral axis of the hull beam. The second part is local deformation, which is the cross-sectional deformation, usually caused by the local load acting on the shell near the bearing.

2.2.1. Global Deformation Calculation

Similar to the calculation of the ship's overall strength, the global deformation calculation simplifies the hull into a thin-walled hollow beam of variable section [29], assuming that the ship is placed statically on the waves and that the change in buoyancy resulting from hull deformation is disregarded. The loads in deformation are calculated in the same way as the strength, considering the balance between gravity and buoyancy. The global deformation calculation can be performed simultaneously with the strength calculation, which is necessary during the design process, thus reducing the workload.

The calculation of global deformation is simplified to the mechanical model depicted in Figure 3. The distributed load ($q(z)$) is the combined forces of gravity and buoyancy (including hydrostatic buoyancy and wave additional buoyancy). F represents the concentrated mass load at various locations. For instance, the weight of bulkheads and equipment corresponds to the concentrated load acting on the hull beam. The head and stern constraints shown in Figure 3 are imposed so that the calculation can be performed. In actuality, the calculated hull beams are in equilibrium, and the reaction forces of the two constraints are both zero.

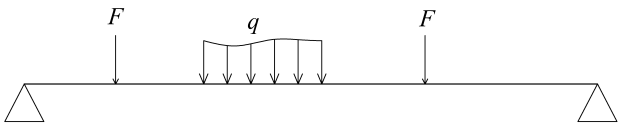

Figure 3. Schematic diagram of the hull beam.

In this paper, the MDM [30] is used to calculate the non-uniform beam—one of several methods available. Initially, the non-uniform hull beam is equated to multiple uniform beams of various dimensions, and Figure 3 becomes Figure 4. e_i represents an element divided according to a certain length, $1 - n + 1$ represents the number of displacement nodes, RF represents the restrained reaction force, and F is the concentrated force at the nodes. The length of the rib spacing is the length of an element, so that concentrated forces can be approximately assigned to the nodes at the end of the element. The distributed loads can be equated to uniform loads.

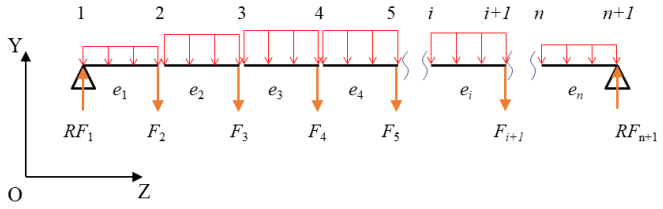

Figure 4. Schematic diagram of the single-span beam model.

The MDM employs nodal displacement as the fundamental unknown quantity and derives equations from the nodal static equilibrium conditions. The crucial step is determining the element stiffness matrix and the global equilibrium equation.

In MDM, the ends of the elements are assumed to be clamp-constrained as shown in Figure 5a. The resultant end force of the element consists of two components: the force due to displacement and the force due to external load, as shown in Figure 5b. According to the static equilibrium condition, the resultant shear force and the resultant bending moment of the nodes are equal to 0. Thus, The equilibrium equation for node i can be expressed as Equation (1).

$$\begin{aligned} \overline{N}_i^{i-1} + \overline{\overline{N}}_i^{i-1} + \overline{N}_i^i + \overline{\overline{N}}_i^i = N_i^{i-1} + N_i^i = 0 \\ \overline{M}_i^{i-1} + \overline{\overline{M}}_i^{i-1} + \overline{M}_i^i + \overline{\overline{M}}_i^i = M_i^{i-1} + M_i^i = 0 \end{aligned} \tag{1}$$

where N stands for the shear force, M stands for the bending moment, the subscripts indicate node number, and the superscripts indicate element number. $\overline{N}_i^i$ and $\overline{M}_i^i$ are the force and bending moment caused by the external load, respectively. $\overline{\overline{N}}_i^i$ and $\overline{\overline{M}}_i^i$ are the force and bending moment caused by the displacement, respectively.

According to the beam theory, the relationship between the force ($\overline{\overline{N}}_i^i$ $\overline{\overline{M}}_i^i$) and the displacement can be expressed as Equation (2).

$$\begin{aligned}
\overline{\overline{N}}_i^i &= \frac{12EI_i}{l_i^3}v_i + \frac{6EI_i}{l_i^2}\theta_i - \frac{12EI_i}{l_i^3}v_{i+1} + \frac{6EI_i}{l_i^2}\theta_{i+1} \\
\overline{\overline{M}}_i^i &= \frac{6EI_i}{l_i^2}v_i + \frac{4EI_i}{l_i}\theta_i - \frac{6EI_i}{l_i^2}v_{i+1} + \frac{2EI_i}{l_i}\theta_{i+1} \\
\overline{\overline{N}}_{i+1}^i &= -\frac{12EI_i}{l_i^3}v_i - \frac{6EI_i}{l_i^2}\theta_i + \frac{12EI_i}{l_i^3}v_{i+1} - \frac{6EI_i}{l_i^2}\theta_{i+1} \\
\overline{\overline{M}}_{i+1}^i &= \frac{6EI_i}{l_i^2}v_i + \frac{2EI_i}{l_i}\theta_i - \frac{6EI_i}{l_i^2}v_{i+1} + \frac{4EI_i}{l_i}\theta_{i+1}
\end{aligned} \tag{2}$$

where E_i is the elasticity modulus of e_i, I_i is the moment of inertia, and l_i is the unit's length. v_i represents the nodal displacement along the Y axis, and θ_i represents the nodal rotation about the X axis.

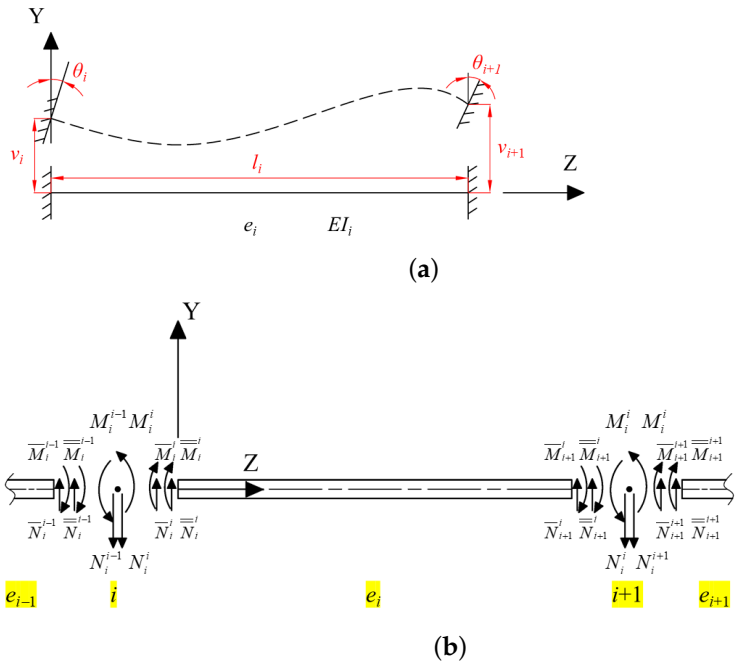

Figure 5. Schematic diagram of deformations and forces in elemental coordinates. (**a**) Deformations; (**b**) forces.

According to Equation (2), the element stiffness matrix ($\boldsymbol{K}^{ei}$) of element e_i is shown in Equation (3).

$$\boldsymbol{K}^{ei} = \frac{E_i I_i}{l_i}\begin{bmatrix} \frac{12}{l_i^2} & \frac{6}{l_i} & -\frac{12}{l_i^2} & \frac{6}{l_i} \\ \frac{6}{l_i} & 4 & -\frac{6}{l_i} & 2 \\ -\frac{12}{l_i^2} & -\frac{6}{l_i} & \frac{12}{l_i^2} & -\frac{6}{l_i} \\ \frac{6}{l_i} & 2 & -\frac{6}{l_i} & 4 \end{bmatrix} \tag{3}$$

The remaining four force components on the left side of Equation (1) due to external loads are still unknown. The external load of each element consists of a uniform line load and a concentrated force at the right end, from which the other four unknown quantities can be expressed as Equation (4). Additionally, the influence of the reaction forces (RF_1 and RF_{n+1}) must be considered for elements e_1 and e_n.

$$\begin{bmatrix} \overline{N}_i^i \\ \overline{M}_i^i \\ \overline{N}_{i+1}^i \\ \overline{M}_{i+1}^i \end{bmatrix} = \begin{bmatrix} \frac{q_i l_i}{2} \\ -\frac{q_i l_i^2}{12} \\ \frac{q_i l_i}{2} + F_{i+1} \\ \frac{q_i l_i^2}{12} \end{bmatrix} \tag{4}$$

Substituting Equations (2) and (4) into Equation (1) yields the force equilibrium equation about node i. Figure 6 depicts the node displacement relationship between multiple elements. Obviously, the force equilibrium equation of a node includes the displacements of two adjacent nodes. By iteratively listing all equilibrium equations for nodes $1 - n + 1$, the final solution equations can be obtained in matrix form, as shown in Equation (5).

$$\boldsymbol{p}_{Total} = \boldsymbol{K}_{Total}\boldsymbol{\delta}_{Total} \tag{5}$$

where $\boldsymbol{K}_{Total}$ is the total element stiffness matrix, $\boldsymbol{p}_{Total}$ is the tatal force vector, and $\boldsymbol{\delta}_{Total}$ is the total displacement vector. They are displayed as Equations (6)–(8).

$$\boldsymbol{p}_{Total} = \begin{bmatrix} -\frac{q_1 l_1}{2} + RF_1 \\ -\frac{q_1 l_1^2}{12} \\ \vdots \\ -\frac{q_{i-1} l_{i-1}}{2} - F_i - \frac{q_i l_i}{2} \\ \frac{q_{i-1} l_{i-1}^2}{12} - \frac{q_i l_i^2}{12} \\ -\frac{q_i l_i}{2} - F_{i+1} - \frac{q_{i+1} l_{i+1}}{2} \\ \frac{q_i l_i^2}{12} - \frac{q_{i+1} l_{i+1}^2}{12} \\ \vdots \\ -\frac{q_n l_n}{2} - F_{n+1} + RF_{n+1} \\ \frac{q_n l_n^2}{12} \end{bmatrix} \tag{6}$$

$$\delta_{Totoal} = \begin{bmatrix} v_1 \\ \theta_1 \\ \vdots \\ v_i \\ \theta_i \\ v_{i+1} \\ \theta_{i+1} \\ \vdots \\ v_{n+1} \\ \theta_{n+1} \end{bmatrix} \tag{7}$$

$$\boldsymbol{K}_{Total} = \begin{bmatrix} K_{11}^{e_1} & K_{12}^{e_1} & K_{13}^{e_1} & K_{14}^{e_1} & & & & & & & & & \\ & K_{22}^{e_1} & K_{23}^{e_1} & K_{24}^{e_1} & & & & & & & & & \\ & & \ddots & & & & & & & & & & \\ & & & & K_{33}^{e_{i-1}} + K_{11}^{e_i} & K_{34}^{e_{i-1}} + K_{12}^{e_i} & K_{13}^{e_i} & K_{14}^{e_i} & & & & & \\ & & & & & K_{44}^{e_{i-1}} + K_{22}^{e_i} & K_{23}^{e_i} & K_{24}^{e_i} & & & & & \\ & & & & & & K_{33}^{e_i} + K_{11}^{e_{i+1}} & K_{34}^{e_i} + K_{12}^{e_{i+1}} & K_{13}^{e_{i+1}} & K_{14}^{e_{i+1}} & & & \\ & & & & & & & K_{44}^{e_i} + K_{22}^{e_{i+1}} & K_{23}^{e_{i+1}} & K_{24}^{e_{i+1}} & & & \\ & & & & & & & & & \ddots & & & \\ & & & & & & & & & & K_{33}^{e_{n+1}} & K_{34}^{e_{n+1}} & \\ & & & & & & & & & & & K_{44}^{e_{n+1}} & \end{bmatrix} \tag{8}$$

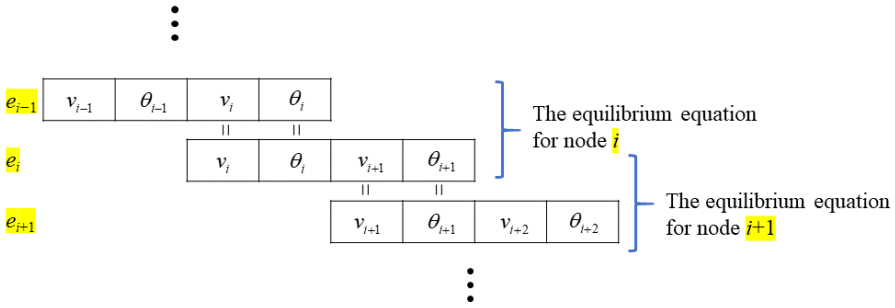

Figure 6. Schematic diagram of relationship between nodal displacement and multiple elements.

In Equation (5), there are two unknown quantities in the force vector on the left, namely RF_1 and RF_{n+1}, whereas v_1 and v_{n+1} correspond to the positions of the simple support points, whose values are both 0, and the remaining $2n$ values are unknown. Consequently, the problem consists of solving $2(n+1)$ equations for $2(n+1)$ unknown quantities using $2(n+1)$ equations, which is plainly straightforward. Using the beam's general solution, other quantities are easily determined after the displacement values of the nodes have been solved.

In terms of the calculation process, the MDM and FEM share many similarities, but they are not identical. First, in terms of the fundamental principle, the MDM solves the displacement linearly by listing the equilibrium equations of force, whereas the FEM solves displacement by assuming the shape function to list the energy equations, solving displacement by the variational method. Second, the MDM is generally applicable to the solution of simpler structures, and the solution speed is rapid, whereas the FEM is applicable to both simple and complex structures, although its modeling and meshing limitations make its computational process relatively complex and time-consuming.

2.2.2. Local Deformation Calculation

In the calculation of global deformation, it is presumed that the deformation of each point of the cross section is identical to the neutral axis of the beam. The local deformation calculation corrects for this assumption. The cabin between two bulkheads is chosen as the range of local deformation analysis, and its load diagram is depicted in Figure 7. Water pressure deforms the bottom plate and a portion of the side plate, while the deformation of the bulkhead position is negligible. Thus, when contemplating local deformation, the bulkhead can be viewed as a form of constraint for the cabin section's intermediate shell. Due to the bulkhead's slight inward compression, the three displacements can be approximated as 0. Considering that the bulkhead is primarily loaded by water pressure, its bending moment does not change abruptly, so the rotation angle can also be regarded as being close to 0. Therefore, the bulkhead can be equated to a clamped support.

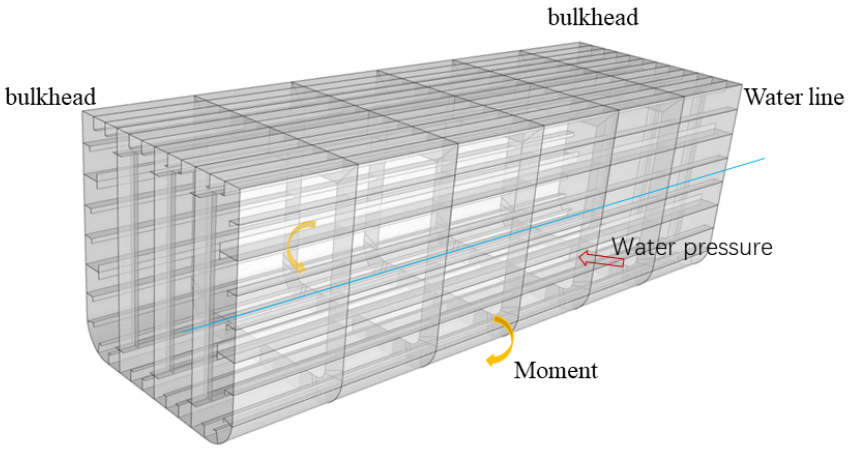

Figure 7. Schematic diagram of the loaded cabin.

The objective of the calculation is to determine the offset and rotation of the bearing on the bottom plate. According to Figure 7, the local deformation can be divided into two parts: the first part is the deformation of the plate with four edges clamped under the transverse pressure load, as depicted in Figure 8a; the second part is the action of the transverse frame when a certain bending moment exists, as depicted in Figure 8b.

The solutions to the two local deformations depicted in Figure 8 are not easy. The FEM [31] is the main method for resolving the first part due to the presence of longitudinal and transverse stiffeners, the non-uniformity of their size and spacing, and the non-uniformity of the load. In the second section, it is challenging to define the section's scope and moment. The local deformation must therefore seek alternative solutions.

The solution does not require the deformation distribution of the entire plate shell but the deformation of the longitudinal and transverse stiffeners, as bearings are typically arranged at the intersection of the longitudinal and transverse stiffeners. Figure 9 illustrates how the plate and shell in the cabin section can be calculated as the equivalent of a grillage beam model.

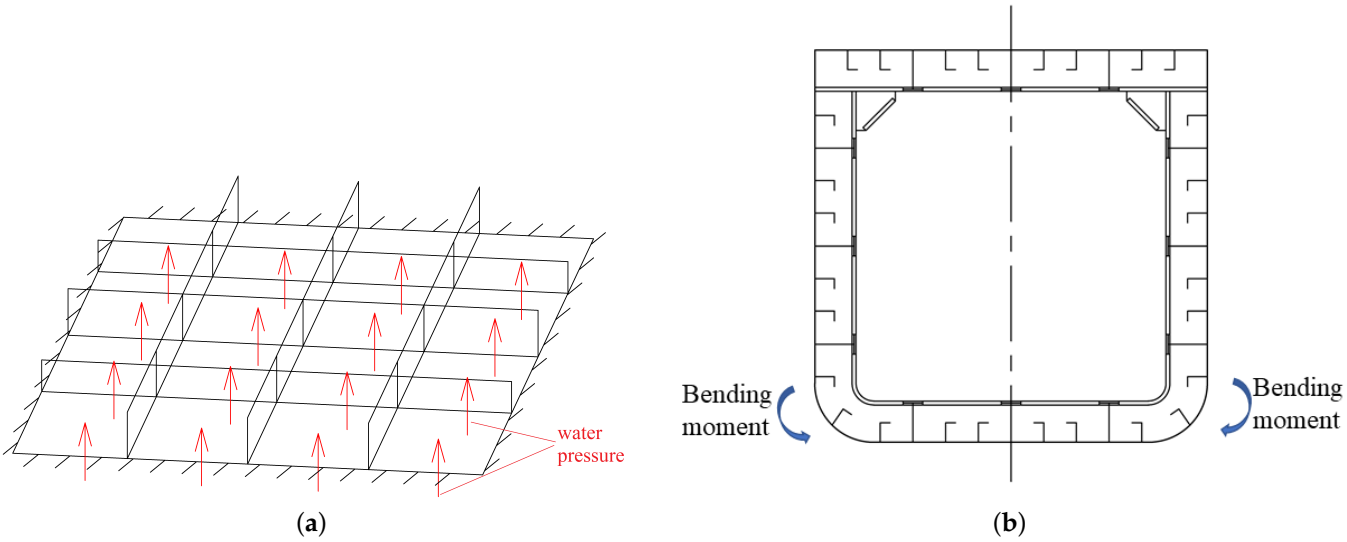

Figure 8. Schematic diagram of the local deformation. (**a**) Four edges clamped plate underwater. (**b**) Transverse frame under bending moment.

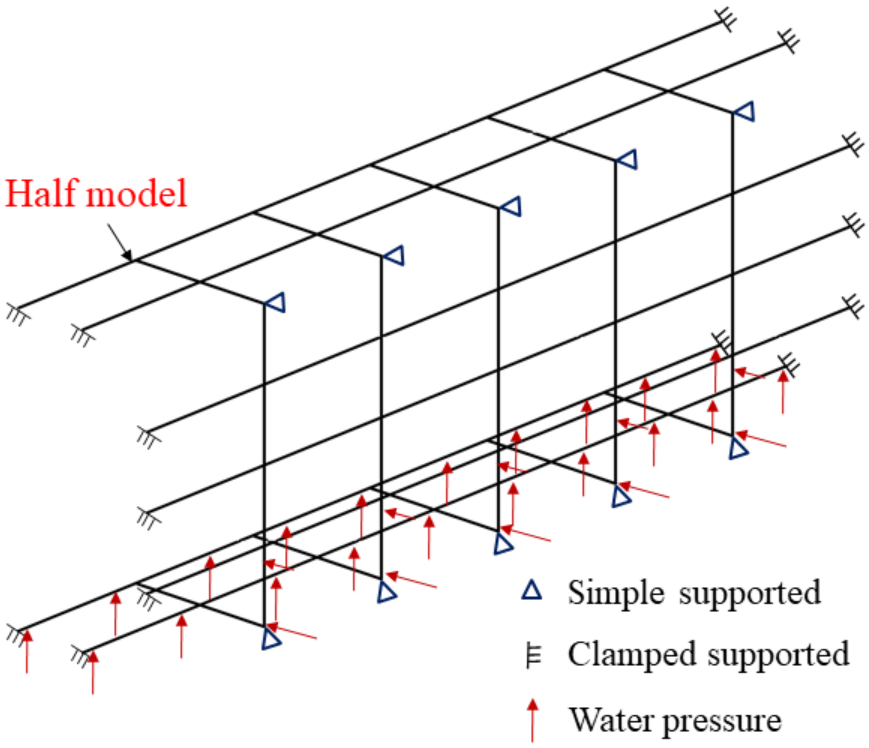

Figure 9. Schematic diagram of the grillage beam model for local deformation calculation.

Model simplification is guided by the following principles:

- The length is bounded by the bulkheads, the breadth by the sides, and the height by the bottom and the deck plate above the waterline;
- Both strong and weak stiffeners need to be established. Because the actual load on the strong stiffeners is closer to the actual circumstances, if both are established, the deformation result is more accurate;
- The bottom frame is only considered to be loaded by the longitudinal stiffeners, and the transverse stiffener load is transferred from the longitudinal stiffeners; the side frame is only considered to be loaded by the transverse stiffeners, as this part primarily affects the transverse bending moment;

- The function of the bulkhead for longitudinal stiffeners is to provide clamped support; the horizontal and vertical intersection nodes of the transverse frame provide simple support;
- When the model is symmetrical, half of the model can be extracted, and symmetrical constraints are applied to the symmetrical surface.

For the solution calculation of the grillage beam model, there are two methods: the FEM and the MDM. The MDM is used in this paper. The spatial location of the beam units in the frame differs from the calculation of the hull beam in the preceding section, resulting in two discrepancies in the calculation. One is that the element stiffness matrix must take into account torsion. In addition, for the global stiffness matrix, the influence of the beam units at various spatial locations must be taken into account.

The beam elements in the space plate frame of Figure 9 have three principal directions—longitudinal along the ship's length, transverse along the ship's width, and vertical along the ship's height—which correspond to the directions of elements e_1, e_2, and e_3, respectively, in Figure 10. Element e_1's rotation around the OX axis at node 2 is equivalent to element e_2's torsion, so the effect of torsion must be accounted for in the element stiffness matrix. As a result, Equation (3) becomes Equation (9).

$$\overline{\boldsymbol{K}^{ei}} = \frac{E_i}{l_i}\begin{bmatrix} \frac{J_{zi}}{2(1+\mu_i)} & 0 & 0 & -\frac{J_{zi}}{2(1+\mu_i)} & 0 & 0 \\ & 4I_i & -\frac{6I_i}{l_i} & 0 & 2I_i & \frac{6I_i}{l_i} \\ & & \frac{12I_i}{l_i^2} & 0 & -\frac{6I_i}{l_i} & -\frac{12I_i}{l_i^2} \\ & & & \frac{J_{zi}}{2(1+\mu_i)} & 0 & 0 \\ & & & & 4I_i & \frac{6I_i}{l_i} \\ & & & & & \frac{12I_i}{l_i^2} \end{bmatrix} \tag{9}$$

where μ_i is Poisson's ratio, and J_{zi} is the polar moment of inertia.

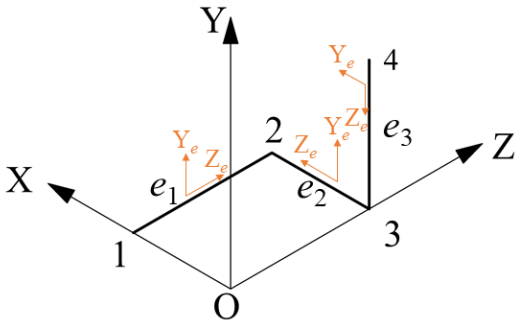

Figure 10. Schematic diagram of the local coordinates of the beam unit.

The element's spatial location and local coordinates are distinct. The trajectory of the local coordinates for the longitudinal, transverse, and vertical beam units is depicted in Figure 10. The local coordinate of element e_1 is aligned with the global coordinate, whereas the local coordinates of elements e_2 and e_3 have an angle with the global coordinate.

Take element e_2 as an illustration of the relationship between the element stiffness matrix and the coordinate transformation matrix ($\boldsymbol{T}^{ei}$). The elemental coordinate of e_2 is rotated by $\alpha_y = +90°$ about the OY axis relative to the global coordinate, with '+' representing the positive direction of the right-handed coordinate. Then, the transformation matrix ($\boldsymbol{T}^{e2}$) is:

$$T^{e2} = \begin{bmatrix} \cos\alpha_y & 0 & -\sin\alpha_y & & & \\ 0 & 1 & 0 & & 0 & \\ \sin\alpha_y & 0 & \cos\alpha_y & & & \\ & & & \cos\alpha_y & 0 & -\sin\alpha_y \\ & 0 & & 0 & 1 & 0 \\ & & & \sin\alpha_y & 0 & \cos\alpha_y \end{bmatrix} = \begin{bmatrix} 0 & 0 & -1 & & & \\ 0 & 1 & 0 & & 0 & \\ 1 & 0 & 0 & & & \\ & & & 0 & 0 & -1 \\ & 0 & & 0 & 1 & 0 \\ & & & 1 & 0 & 0 \end{bmatrix} \tag{10}$$

As a result, the element stiffness matrix of e_2 in the global coordinate can be expressed as:

$$\boldsymbol{K}^{e2} = \boldsymbol{T}^{e2}\overline{\boldsymbol{K}^{e2}}\boldsymbol{T}^{e2T} \tag{11}$$

where $\boldsymbol{T}^{e2T}$ is the transpose matrix of $\boldsymbol{T}^{e2}$, and the two are inverse matrices of each other.

The subsequent calculation then follows the same procedure as the previous section, i.e., the element stiffness matrices are assembled into the total stiffness matrix; then, the solution is calculated using Equation (5).

In general, when the local coordinate has α_x, α_y, and α_z angles with the X, Y, and Z axes of the global coordinate, respectively, the coordinate transformation matrix can be expressed as Equation (12).

$$\boldsymbol{T}^{ei} = \boldsymbol{T}_{\alpha z}\boldsymbol{T}_{\alpha y}\boldsymbol{T}_{\alpha x} \tag{12}$$

where $\boldsymbol{T}_{\alpha x}$, $\boldsymbol{T}_{\alpha y}$, and $\boldsymbol{T}_{\alpha z}$ represent the transformation matrix corresponding to α_x, α_y, and α_z, respectively.

3. Verification of Hull Deformation Calculation

To verify the accuracy of the proposed method, a static floating box beam model is calculated using both the FEM and the proposed method. Table 1 demonstrates the parameters associated with the box beam. The box beam model includes three bulkheads in the middle and employs a longitudinal system of framing. All the strong stiffeners are uniformly made of flat steel with dimensions of 8 mm × 250 mm, and the weak stiffeners are made of flat steel with dimensions of 8 mm × 100 mm. It is assumed that the box beam is statically floating on the water, and its total weight is 269 tons with a draft of 336.2 mm.

Table 1. Geometric parameters of the box beam.

Parameter	Number	Parameter	Number
Length (m)	100	Strong stiffener (mm)	8 × 250
Breadth (m)	8	Weak stiffener (mm)	8 × 100
Height (m)	8	Frame spacing (m)	2.5
Thickness (mm)	8	Longitudinal spacing (m)	1.0

The box beam depicted in Figure 11 was established in ANSYS with the length in the Z direction, the width in the X direction, and the height in the Y direction. The SHELL281 element is utilized for both the plate and stiffeners. The element size is set to 250 mm, and Figure 12 depicts both the geometry and the mesh model of the local structure. When the division of elements is finished, there is a total of 88,200 elements. Checking the quality of the elements revealed none to be defective, indicating that the FEM calculation yields an accurate result. At the midpoint of the bow deck, three directional degrees of freedom are constrained in X, Y, and Z directions; at the midpoint of the stern deck, two directional degrees of freedom are constrained in the Y and Z directions; and at the side point of the stern deck, Y directional degrees of freedom are constrained.

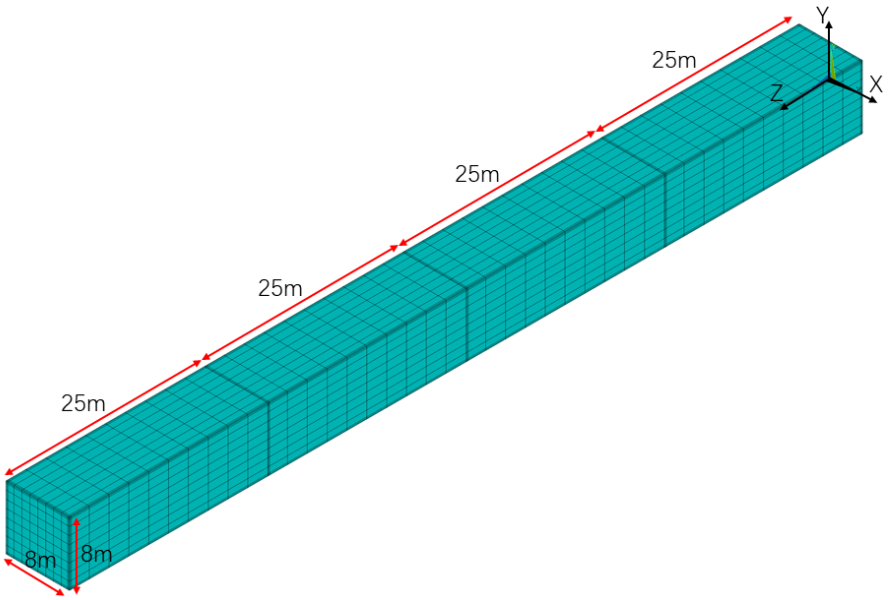

Figure 11. Geometric model of the box beam.

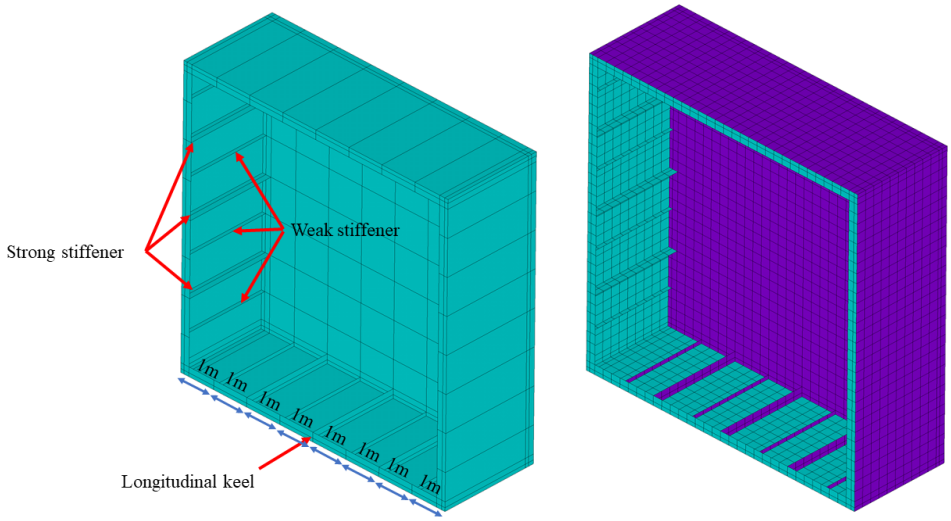

Figure 12. Diagram of the local structure of the box beam. (**a**) Geometry model. (**b**) Mesh model.

After the calculation is complete, the longitudinal keel's displacement (U_y) and rotation angle (R_x) are extracted and contrasted with the calculation results of the proposed method. Figure 13a depicts a comparison of U_y, where the dashed line represents the FEM result and the solid line with red circular symbols represents the sum of the global and local deformations. The results of the two methods are comparable in both magnitude and trend. The displacement of the middle longitudinal keel exhibits a periodic half-sine waveform along the longitudinal axis. The period is 0.25 L, and the three positions of 0.25 L, 0.5 L, and 0.75 L correspond to the three bulkhead positions, thereby validating the assumption of using the bulkhead as the boundary of local deformation.

The solid blue line in Figure 13a represents the global deformation, which has an arch shape with a maximum value of 1.25 mm and is significantly less than the result of the sum of the displacements (local + global). This is due to the shallow draft of the box beam and the small global longitudinal moment. Compared to a typical ship, the box beam's stiffeners are sparse and tiny in size, so the local deformation is greater. This is done on purpose because global deformation calculations using the single-span beam model are widely used, whereas local deformation calculations using the grillage beam model

are uncommon. By enlarging the local deformation, the accuracy of the method used to calculate the local deformation can be more clearly observed.

Figure 13b depicts a comparison of the results of the rotation angle. It shows that the FEM results are very similar to those obtained with the proposed method. In one cycle, the rotation angle of the longitudinal keel demonstrates a complete sinusoidal wave pattern, with the bulkhead serving as the boundary. This demonstrates that when considering the influence of local deformation on the bearing's angle, the results vary depending on the position of the bearings in the cabin. The comparison demonstrates the reliability of the proposed method.

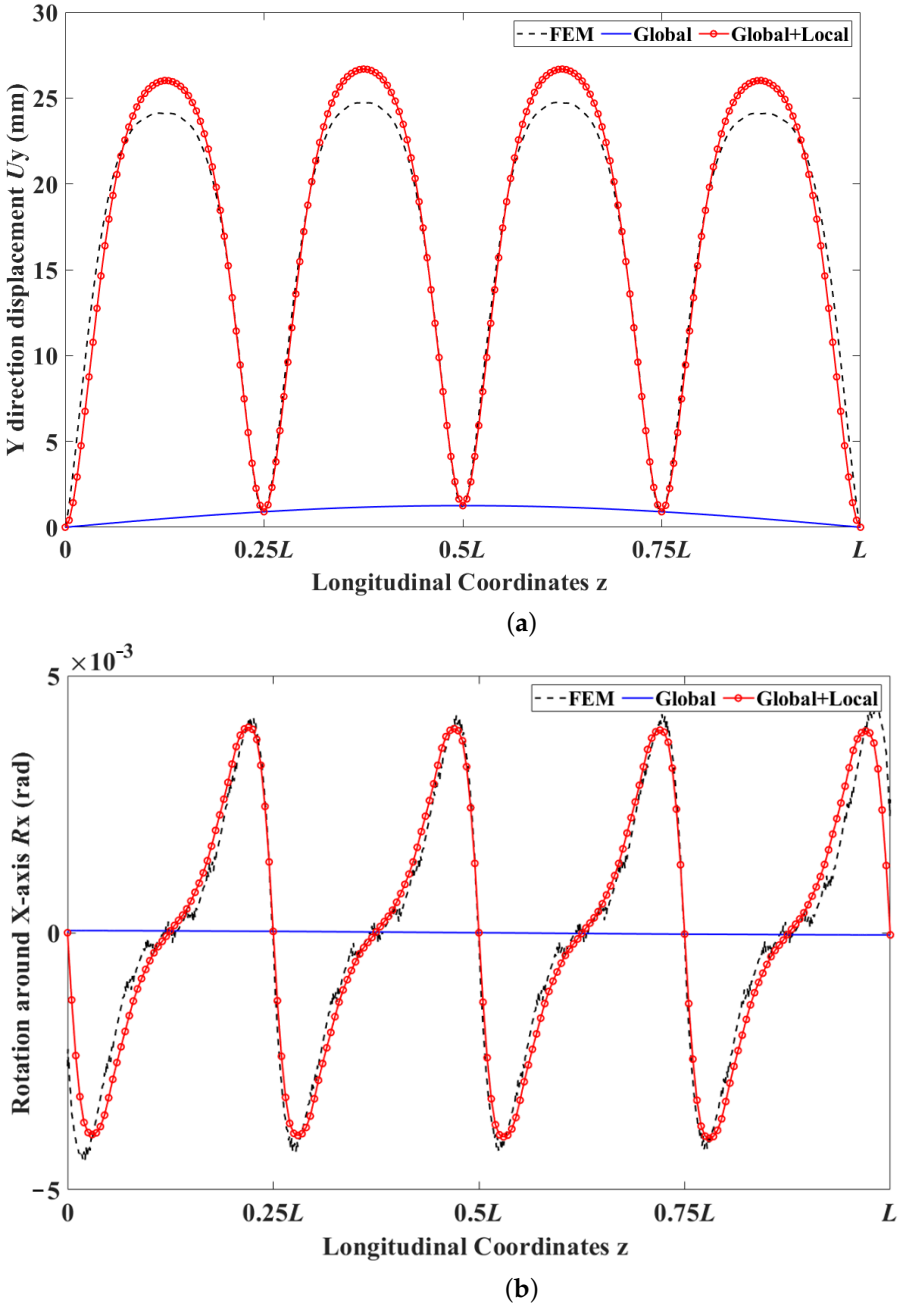

Figure 13. Results comparison with the FEM. (**a**) Displacement comparison. (**b**) Rotation comparison.

The difference in the results presented the two figures above is mainly due to the simplification of the hull deformation into two beam models when using the MDM. However, the small deviation shows that the result is acceptable. Although the FEM calculation

may be more accurate, the MDM method requires only a few hours for modeling and calculations, whereas the FEM calculation requires several weeks to create a complete hull model. Therefore, MDM has a distinct advantage for extensive computational work like optimizing hull structure.

4. Case Study of the Effect of Hull Deformation on Shaft Alignment

In analyzing the impact of hull deformation on shaft alignment, the internal pressure change of the bearing is the main concern. The entire calculation consists of three stages, with the calculation flow depicted in Figure 14. The first step is to calculate the hull deformation under various loading and wave conditions; the second step is to input the bearing offset and rotation into the shaft alignment calculation in order to calculate the bearing reaction force and shaft deflection curve; and the third step is to calculate the internal pressure of the bearing based on the bearing load value and the relative angle between the bearing and the shaft. The second section of this paper describes the first-step calculation of the hull deformation. The method of calculation for the second and third stages can be found in Ref. [22] and Ref. [24], respectively. In the third stage, there are two pressure cases corresponding to the initial start/stop and continuous operation of the shaft system, namely static contact pressure and dynamic hydrodynamic pressure. This paper focuses primarily on the contact pressure and uses it as a parameter to evaluate the bearing's response to hull deformation.

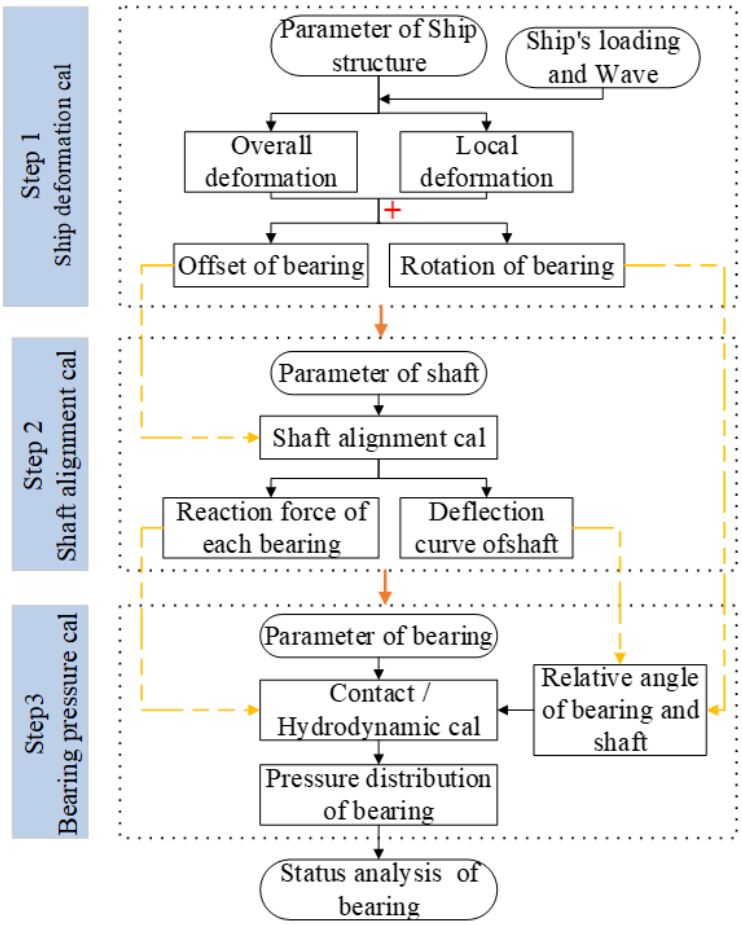

Figure 14. The calculation flow chart for the effect of hull deformation on shafting bearings.

4.1. Introduction of the Ship Layout and the Calculation Working Conditions

As the subject of analysis, a vessel with bearing failure is selected. Figure 15 depicts the stern layout of the vessel. The propulsion shaft system is located in the middle longitudinal section. There are seven bearings in this ship, and the rear three are water-lubricated

Thordon bearings. The material parameters of Thordon bearings are referred to in Ref. [24]. The front four bearings are white alloy bearings that are lubricated with oil, and they are all located inside the cabin. The bearing parameters are shown in Table 2.

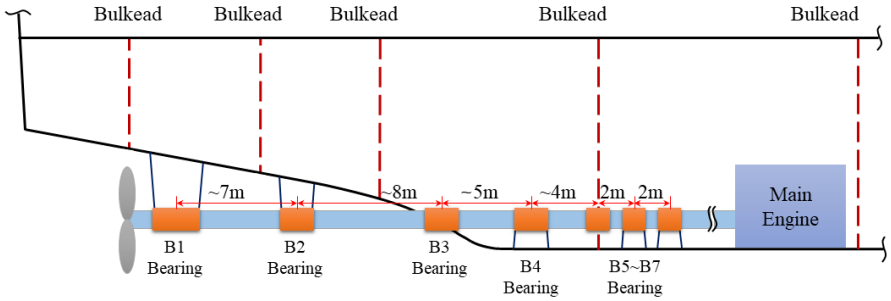

Figure 15. Stern layout of the vessel.

Table 2. Table of bearing parameters.

Bearing No.	Material	Length-to-Diameter Ratio
B1	Thordon	1:2
B2	Thordon	1:1.5
B3	Thordon	1:1
B4–B7	White metal	1:1

Ship loading and waves are two key factors that affect hull deformation. Many combinations of the two exist, and several typical working conditions are selected for analysis, as listed in Table 3. Initial consideration is given to the loading variation in still water, including the variation from light load to constant load to full load. Then, distinct wave conditions are considered, assuming that the loading is always constant. It is presumed that waves are two-dimensional cosine waves with a wavelength equal to the ship's length and the crest-to-trough height variation. The ship is hogging when the wave phase of 0° is located at the stern and is sagging when the wave phase of 90° is located at mid-ship.

Table 3. Table of the working conditions.

Wave	Loading	Nominal Wave Height
Still	Light/Constant/Full	0.0 (m)
Hogging	Constant	0.1/0.5/1.25/2.5/4.0/6.0 (m)
Sagging	Constant	0.1/0.5/1.25/2.5/4.0/6.0 (m)

4.2. Comparison of Different Loadings in Still Water

A comparison of the global hull deformation for different loadings in still water is shown in Figure 16. The vertical lines in the picture show the locations of bearings B1–B7 from left to right. When the loading changes, the hull deforms significantly. The bearings in different positions are correspondingly deflected and rotated. From the light load to the full load, the offset value of the B1 bearing changes the least, and the rotation value changes the most, reaching 1.5×10^{-3} rad. The rotation value of the B7 bearing changes the least, and the offset value changes the most, reaching -50 mm.

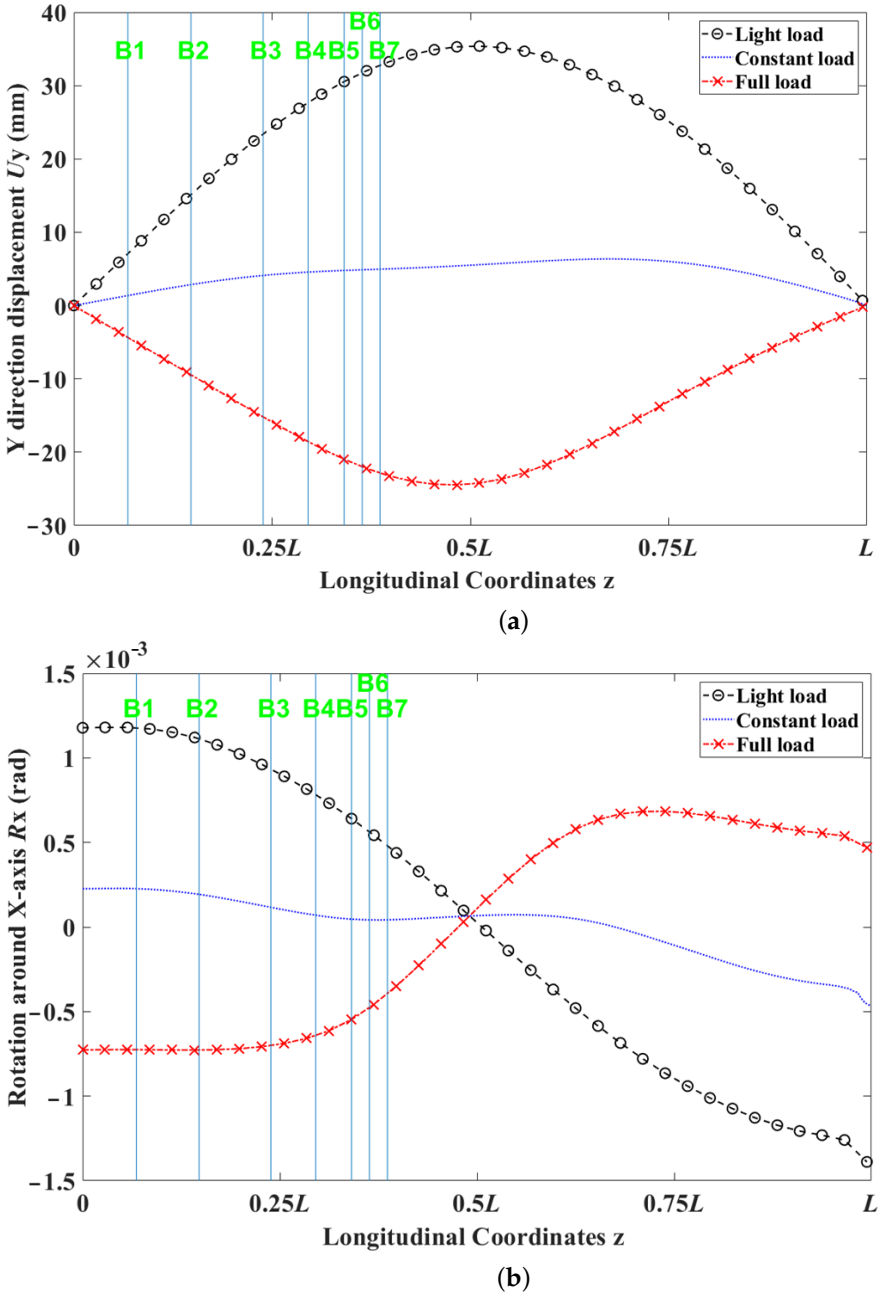

Figure 16. Comparison of the global deformation at different loadings in still water. (**a**) Vertical displacement. (**b**) Rotation angle.

The local deformation results for the three loads in still water are shown in Figure 17. The local deformation is calculated over four cabin lengths, covering seven bearings and containing five bulkheads. The long vertical lines are used to identify the bulkhead locations, and the short vertical lines are used to identify the bearing locations. The local deformation results exhibit periodicity according to the bulkhead boundary. The displacement results show a periodic half-sine waveform, and the rotation results show a periodic sine waveform. The results indicate that there are variations in the local displacement and rotation based on the bearing's positioning within the cabin. Although the results presented in Figure 17 correspond to still-water conditions, it is reasonable to infer that the local deformation trends would be analogous in wave conditions, given the fact that water pressure remains relatively consistent within the same cabin.

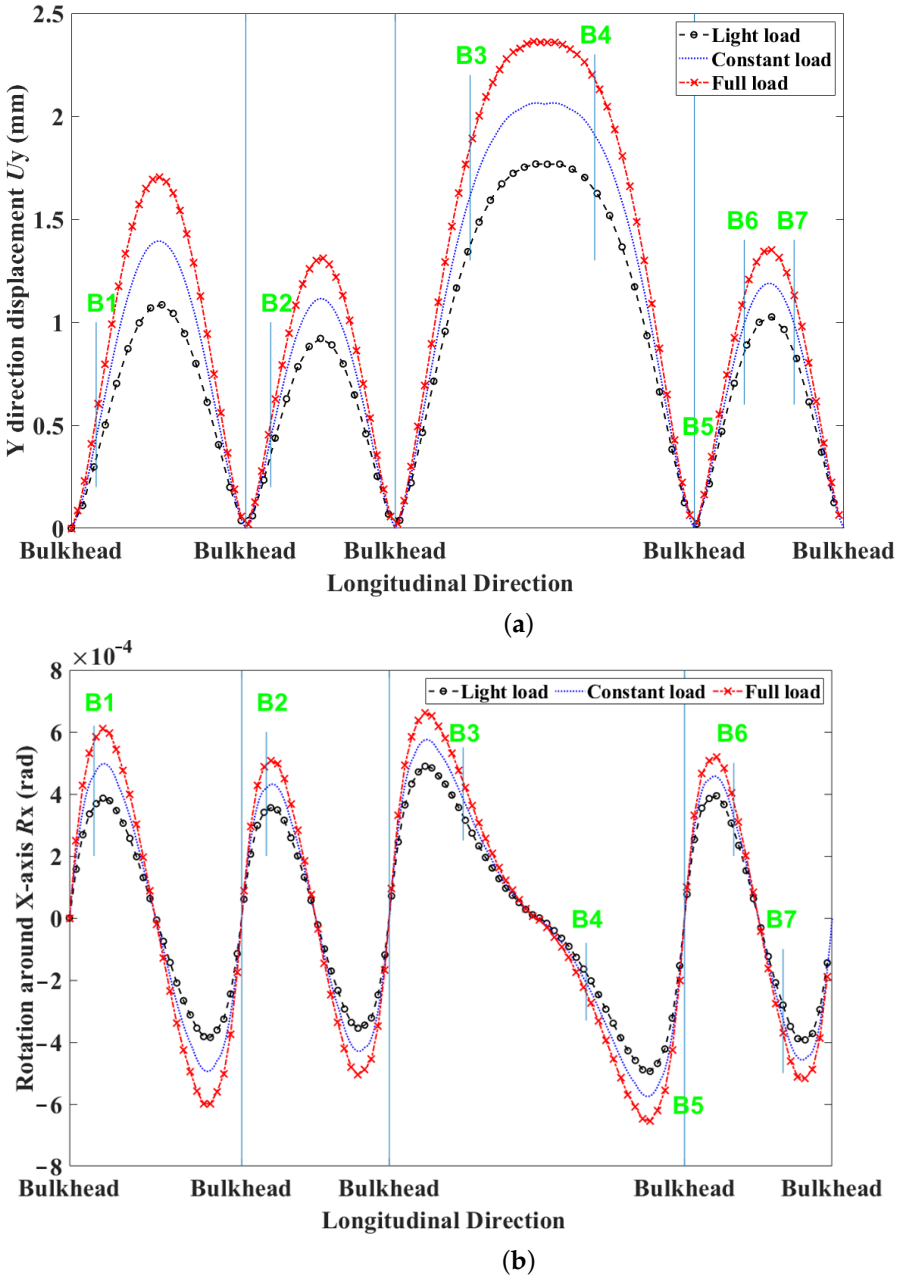

Figure 17. Comparison of the local deformation of the hull at different loadings in still water. (**a**) Vertical displacement. (**b**) Rotation angle.

By comparing Figures 16 and 17, it is found that the global deformation exhibits a displacement change magnitude of 10 mm and a rotation change magnitude of 10^{-4} rad. However, the local deformation displays a displacement change magnitude of 1 mm, which is 1/10 of the global deformation, and a rotation change magnitude of 10^{-4} rad, which is comparable to the global deformation. However, the difference in displacement values does not indicate that the local deformation has a minimal impact on the shaft system because global deformation includes rigid body displacement, which has no influence on the shaft system.

According to the bearing offset and rotation values, the shaft alignment calculation and bearing pressure calculation can be carried out according to step 2 and step 3 in Figure 14, respectively. The analysis primarily focuses on the three stern bearings, namely B1, B2, and B3, due to their nearness to the propeller, resulting in a relatively larger load. The results are listed in Table 4. The base condition is required in the shaft alignment

calculation, since the results of the hull deformation are relative values rather than absolute values. Considering the process of shaft installation, it is necessary to perform a secondary adjustment of the shaft system while it is in a floating condition with a light load during the installation process. The base condition is the light load condition, in which the bearing offset is 0mm and the shaft-to-bearing angle is 0 rad. All the shaft alignment and bearing pressure calculations are based on the base condition.

Table 4. Results of bearing reaction force and pressure at different loadings in still water.

Work Condition	Bearing No.	Offset (mm)	Reaction Force (kN)	Shaft-to-Bearing Angle (rad)	Maximum Contact Pressure (MPa)
Light load	B1	0.0	50.69	0.0	1.98
	B2	0.0	38.89	0.0	2.14
	B3	0.0	29.05	0.0	3.30
Constant load	B1	−5.61	50.81	7.8×10^{-5}	2.85
	B2	−12.21	38.76	4.4×10^{-5}	2.48
	B3	−19.05	28.94	5.3×10^{-5}	3.76
Full load	B1	−11.23	50.94	1.7×10^{-4}	3.74
	B2	−24.43	38.62	9.8×10^{-5}	2.89
	B3	−38.10	28.83	1.0×10^{-4}	4.19

It can be seen from Table 4 that although there is a large offset of the bearing, the change in the reaction force of the bearing is small. There are two causes for this phenomenon. The first is that the deformation of the entire shaft is primarily rigid body-like translation and rotation as demonstrated by the nearly straight line of the hull–stern deflection curve in Figure 16a. The second reason is that the three bearings are separated by a significant distance, resulting in a small load variation caused by bearing deflection.

The maximal contact pressure of the three bearings increases as the load increases from light to constant to full. The pressure that changed the most doubled in magnitude. This is due to the change in shaft-to-bearing angle. From the load change and pressure change of the bearing, it is evident that the single load parameter cannot accurately represent the influence of hull deformation on shaft alignment. In order to account for the change in bearing condition during this procedure, another quantity, i.e., shaft-to-bearing angle, is required.

4.3. Comparison of Different wave Conditions

The results depicted in Figures 18–20 can be derived by calculating the wave conditions listed in Table 3. Among them, Figure 18 depicts the variation curves of the three bearings' reaction forces under various wave conditions. It can be observed that as the nominal wave height increases, the change in reaction force of the B3 bearing is the greatest, the change of the B2 bearing is relatively small, and the change of the B1 bearing is the smallest. The bearing reaction force is influenced by the bearing's offset, which consists of two components: the global deformation offset and the local deformation offset. Since the displacement of the shaft in the global deformation includes rigid body translation and rotation, it is difficult to directly compare the effect of global and local deformation on the bearing reaction force.

Figure 19a depicts the variation of the maximum contact pressure inside the bearing when hogging occurs. The curve of the three bearings can be divided into three stages. In the first stage, when the wave height is 0 m–0.5 m, the pressure decreases; in the second stage, when the wave height is 0.5 m–4.0 m, the pressure increases; and in the third stage, when the wave height is 4.0 m–6.0 m, the pressure varies steadily. Comparing Figure 19a to Figure 18a, it is evident that the change in reaction force and the change in bearing pressure are not synchronized. For instance, the reaction force of bearings B1 and B2 remains

essentially unchanged, whereas the bearing's pressure continues to vary with the wave height, and the pressure of bearing B3 increases when the reaction force decreases. This also indicates that in the shaft alignment analysis, the reaction force alone is not sufficient to reflect the change in the bearing condition.

Figure 20 shows the variation curves of the shaft-to-bearing angles and local rotation angles of the three bearings under different wave conditions. The shaft-to-bearing angle depicted in Figure 20a, represented by the three labeled lines (B1, B2, and B3—shaft-to-bearing angle), can explain the cause of the bearing pressure variation depicted in Figure 19a. When the wave height is 0 m–0.5 m, the three bearings' shaft-to-bearing angles transform from negative to positive values. A negative value of the shaft-to-bearing angle indicates that the bearing is aft trim and that the maximum pressure is located at the rear end, whereas a positive value indicates that the bearing is forward trim and that the maximum pressure is located at the front end. When the wave height is between 0.5 m and 4.0 m, the angle of the three bearings progressively increases, which is caused by the wave-induced increase in hull deformation. When the wave height is between 4.0 m and 6.0 m, the B1 and B2 shaft-to-bearing angles remain relatively unchanged, while the B3 angle continues to increase at a decreasing rate. This indicates that the shaft-to-bearing angle does not always increase as the hull deformation increases.

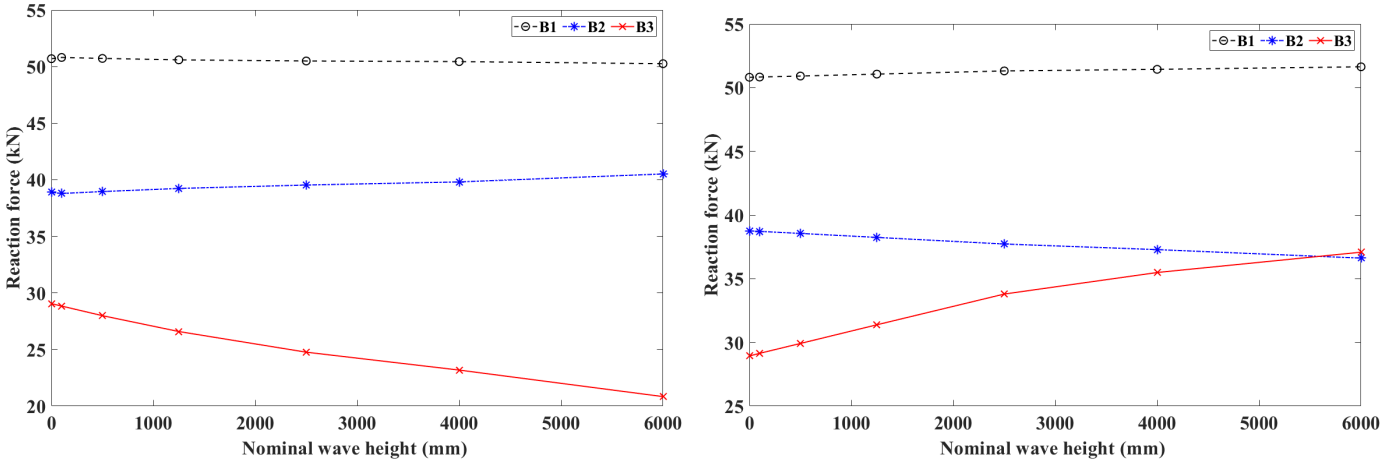

Figure 18. Bearing reaction force variation curve with different wave heights. (**a**) Hogging condition. (**b**) Sagging condition.

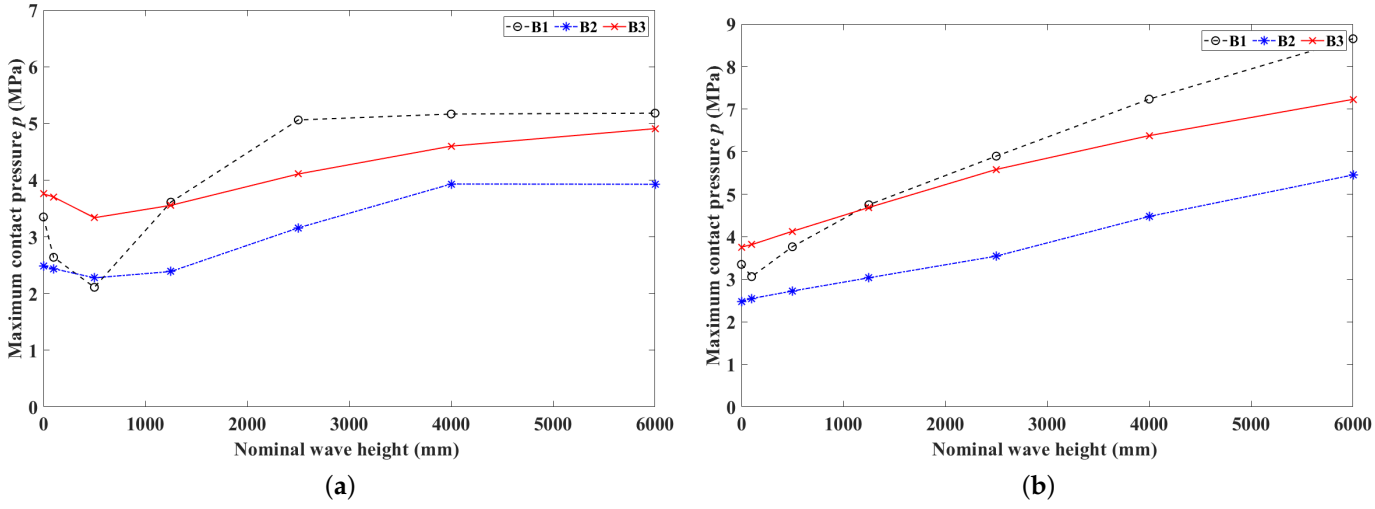

Figure 19. Comparison of the bearing maximum pressure with different wave heights. (**a**) Hogging condition. (**b**) Sagging condition.

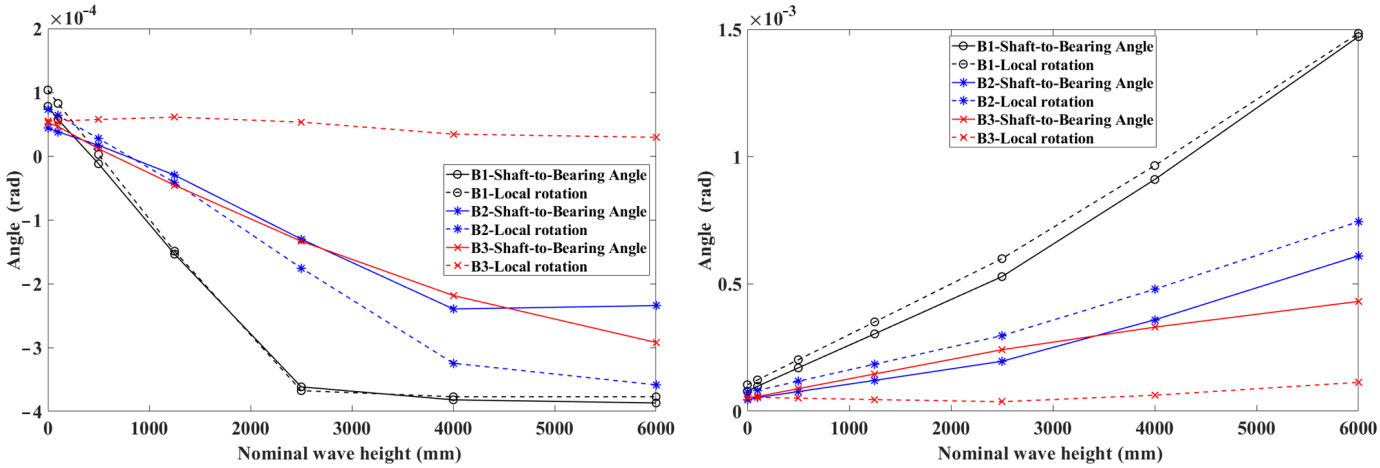

Figure 20. Comparison of local deformation rotation and shaft-to-bearing angle with different wave heights. (**a**) Hogging condition. (**b**) Sagging condition.

The three dashed lines in Figure 20a represent the local rotation curves of the three bearings, i.e., the three lines labeled B1, B2, and B3—local rotation. The local rotation values are obtained in the local coordinate system and are independent of the rigid body's rotation. The shaft-to-bearing angle is also independent of the rigid body displacement. Consequently, these two values are comparable. The influence of the effect of local deformation on shaft-to-bearing angle can be seen from the closeness of the two curves at the same bearing position. The closer the two curves are, the greater the influence of local deformation, and vice versa, the greater the influence of global deformation. In Figure 20a, the two curves of bearing B1 are very close, the two curves of bearing B2 are closer but have some differences, and the two curves of bearing B3 have a significant difference. This indicates that bearing B1 is primarily affected by local deformation, bearing B2 is affected by both global and local deformation, and bearing B3 is primarily affected by global deformation.

Figures 19b and 20b represent the results of the sagging condition, which lacks the first and third stages observed in the hogging condition. The reason for the absence of the first stage is that the shaft-to-bearing angle does not alternate between positive and negative values as the wave height increases in the sagging condition. The absence of a third stage is due to the fact that in the sagging condition, the water line of the bow and stern is higher than the water line of amidships, so the water pressure of bearings B1 and B2 corresponding to local deformation can always increase with the height of the wave. During hogging, the waterlines of the bow and aft are lower than the mid-ship waterline. As the wave height increases, the ship's bottom is elevated above the water for a period of time, resulting in constant local deformation. Comparing the shaft-to-bearing angle curve and the local deformation rotation curve in Figure 20b, it can be seen that the two curves are closest for bearing B1, followed by bearing B2, and have the greatest difference for bearing B3, which is similar to the hogging condition.

From the magnitude of the influence of local deformation and global deformation on bearing pressure, it is easy to draw conclusions for optimization of bearing pressure. For the bearings affected by large local deformation, such as the B1 and B2 bearings, it is necessary to strengthen the local structural stiffness; for the bearings affected by large global deformation, such as the B3 bearing, it is necessary to strengthen the global stiffness of the hull structure. When contemplating the optimization of bearing pressure by adjusting the arrangement, the local deformation-affected bearings can be reduced in this manner. Referring to Figure 17b, the change in the local deformation angle corresponding to various cabin positions differs. For example, the rotation angle in the middle of the compartment is always close to 0, and the greatest change in position occurs near 1/5 of the cabin's length.

Adjusting bearings B1 and B2 to a position close to the compartment's midsection can reduce the local deformation angle, thereby achieving the goal of reducing bearing pressure.

5. Conclusions

This paper studies the effect of hull deformation on shaft alignment. The global deformation and the local deformation are separated, simplified to a single-span beam model and a grillage beam model, respectively, and solved with the MDM. First, the proposed method is applied to a box beam and contrasted with the FEM to evaluate its effectiveness. Then, it is used in a case study to analyze the hull deformation of a ship under various conditions and its effect on the shafting bearings. The conclusions are as follows:

1. Comparing the results of the proposed method and the FEM in the calculation of the box beam reveals that the displacement and rotation trends are highly consistent, and the maximum error of both quantitative values is approximately 10%, demonstrating the validity of the method. In addition, the proposed method omits the FEM's complex modeling, which can substantially reduce workload and time consumption.
2. The influence of hull deformation on shaft alignment is calculated for a ship subject to varying loads and wave conditions, and it is found that with varying hull deformation, some of the bearing forces remain constant while the pressure varies. This indicates that the bearing reaction force is insufficient for evaluation of the bearing condition.
3. The variation in the bearing pressure is consistent with the trend of the shaft-to-bearing angle, indicating that the pressure is affected by the angle. The shaft-to-bearing angle is proposed as an additional evaluation parameter in shaft alignment analysis.
4. Comparing the local rotation and shaft-to-bearing angle reveals that bearings in various positions produce distinct results. This indicates that global and local deformations have different effects on bearings in varying positions. This is crucial for optimizing the design of the vessel structure and bearing arrangement to reduce bearing pressure.
5. The displacement results for the longitudinal local deformation at the cabin bottom exhibit a half-cosine waveform, while the rotation angle results exhibit a full-sine waveform. This suggests that the influence of local deformation can be diminished on bearings that are primarily affected by local deformation by adjusting the longitudinal location of the bearing in the cabin.

In future work, the effect of hull rigidity on shafting vibration can be analyzed, and the effect of hull deformation on the hydrodynamic pressure distribution within the bearing can be discussed.

Author Contributions: Conceptualization, W.Z. and Y.Z.; methodology, W.Z. and Y.Z.; software, W.Z.; validation, H.Y., Y.Z. and X.W.; formal analysis, H.Y.; investigation, X.W.; resources, X.W.; data curation, W.Z.; writing—original draft preparation, W.Z.; writing—review and editing, W.Z.; visualization, H.Y.; supervision, Y.Z.; project administration, H.Y. All authors have read and agreed to the published version of the manuscript.

Funding: This research received no external funding.

Institutional Review Board Statement: Not applicable.

Informed Consent Statement: Not applicable.

Data Availability Statement: Not applicable.

Conflicts of Interest: The authors declare no conflicts of interest.

Abbreviations

The following abbreviations are used in this manuscript:

MDM	Matrix displacement method
FEM	Finite element method

References

1. Low, K.H.; Lim, S.H. Propulsion shaft alignment method and analysis for surface crafts. *Adv. Eng. Softw.* **2004**, *35*, 45–58.
2. Zhou, R.P. The Theoretic Studies on the Propulsion Shafting Alignment of Ultra-Large Vessels. Ph.D. Thesis, Wuhan University of Technology, Wuhan, China, 2005.
3. Sheng, Z.; Liu, Y. *Ship Theory*, 2nd ed.; Shanghai Jiaotong University Press: Shanghai, China, 2015.
4. Acanfore, M.; Balsamo, F. On the development of fast numerical methods for the estimation of hull girder loads for a flooded ship in waves. *Ocean. Eng.* **2021**, *233*, 1–10.
5. Timoshenko, S.P.; Goodier, J.N. *Theory of Elasticity*, 3rd ed.; Higher Education Press: Beijing, China, 2013.
6. Wang, X. *Finite Element Method*, 1st ed.; Tsinghua University Press: Beijing, China, 2003.
7. Murawski, L. Shaft line alignment analysis taking ship construction flexibility and deformations into consideration. *Mar. Struct.* **2005**, *18*, 62–84.
8. Shi, L.; Xue, D.; Song, X. Research on shafting alignment considering ship hull deformations. *Mar. Struct.* **2010**, *23*, 103–114.
9. Seo, C.; Jeong, B.; Kim, J.; Song, M.; Noh, J.; Lee, J. Determining the influence of ship hull deformations caused by draught change on shaft alignment application using FE analysis. *Ocean. Eng.* **2020**, *210*, 107488.
10. Zhang S.; Long, Z.; Yang, X. Reaction force of ship stern bearing in hull large doformation based on stochastic theory. *Int. J. Nav. Archit. Ocean. Eng.* **2020**, *12*, 723–732. [CrossRef]
11. Yu, Y.; Lin, Y.; Li, K.; Ming, C. Buoyancy coupling with structural deformation analysis of ship based on finite element method. *Ocean. Eng.* **2016**, *121*, 254–267.
12. Guo, P. The Method of Rational Alignment and Load Measurement Technology of Propulsion Shafting. Master's Thesis, Shanghai Jiao Tong University, Shanghai, China, 2020.
13. Lee, J. Application of strain gauge method for investigating influence of ship shaft movement by hydrodynamic propeller forces on shaft alignment. *Measurement* **2018**, *121*, 261–275. [CrossRef]
14. Yu, Y.F. Research on Dynamic Alignment Method of Ship Propulsion Shafting Considering Hull Deformation. Master's Thesis, Dalian University of Technology, Dalian, China, 2020.
15. Lee, J.; Jeong, B.; Tae-Hyun, A. Investigation on effective support point of single stern tube bearing for marine propulsion shaft alignment. *Mar. Struct.* **2019**, *64*, 1–17. [CrossRef]
16. Cheng, J.W.; Bu, W.J.; Shi, L.; Fu, J.Q. A real-time shaft alignment monitoring method adapting to ship hull deformation for marine propulsion system. *Mech. Syst. Signal Process.* **2023**, *197*, 1–25. [CrossRef]
17. DNV GL. Incomplete propeller immersion risk of propeller shaft bearing damage. *Tech. Regul. News* **2017**, *1*, 1–3.
18. Hirani, H.; Verma, M. Tribological study of elastomeric bearings for marine propeller shaft system. *Tribol. Int.* **2009**, *42*, 378–390. [CrossRef]
19. Xu, Y.; Zhou, R.P.; Hu, Y.F. Research on influencing factors of stern bearing load distribution. *China Shiprep.* **2019**, *32*, 18–21.
20. ABS. Guidance Notes on 'Guidance Notes on Propulsion Shafting Alignment'. Available online: https://ww2.eagle.org/content/dam/eagle/rules-andguides/current/design_and_analysis/128_propulsionshaftalignment/shaft-alignment-gn-sept-19.pdf (accessed on 1 July 2021).
21. Bureau Veritas (BV). Elastic Shaft Alignment. Available online: https://marine-offshore.bureauveritas.com/nr592-elastic-shaft-alignment-esa (accessed on 1 April 2015).
22. CCS. Part 3 Main and Auxiliary Machinery, Chapter 12 shaft vibration and alignment. In *Rules for the Construction of Domestic Sailing Sea Vessels*; CCS: Beijing, China, 2018.
23. Lloyd's Register. Rules and Regulations for the Classification of Ships. Available online: https://www.lr.org/en/rules-andregulations-for-the-classification-of-ships/(accessed on 1 July 2021).
24. Zhou, W.X.; Zhao, Y.; Yuan, H.; Liu, J.X.; Wang, X.Q. Research on the Contact Pressure Calculation Method for the Misaligned Elastomeric Journal Bearing. *J. Mar. Sci. Eng.* **2022**, *10*, 141. [CrossRef]
25. Lv, F.; Ta, N.; Rao, Z. Analysis of equivalent supporting point location and carrying capacity of misaligned journal bearing. *Tribol. Int.* **2017**, *116*, 26–38. [CrossRef]
26. Ouyang, W.; Liu, Q.; Xiao, J.; Huang, J.; Zhang, Z.; Wang, L. Experimental study on the distributed lubrication characteristics of full-size water-lubricated stern bearings under hull deformation. *Ocean. Eng.* **2023**, *267*, 2–12. [CrossRef]
27. Magalhães, D.; Martins, D.; Castro, B.; Vaz, L.; Monteiro, U.; Gutiérrez, R. Machine learning performance comparison for main propulsive shafting systems alignment. *Ocean. Eng.* **2023**, *280*, 114556. [CrossRef]
28. Zhang, X.; Gu, X. Influence of misalignment angle error on the load-bearing properties of shafting bearing. *Ship Sci. Technol.* **2017**, *39*, 97–102.
29. Wang, J.D.; Yang, Y.Y. *Hull Strength and Structure Design*, 1st ed.; National Defense Industry Press: Beijing, China, 1995; pp. 51–146.

30. Shu, H.Y.; Tan, L.S. *Ship Structural Mechanics*, 1st ed.; Huazhong University of Science and Technology Press: Wuhan, China, 2009; pp. 51–101.
31. Zhang, T.; Liu, T.G.; Zhao, Y. Large deflection analysis of stiffened plates. *Shipbuild. China* **2001**, *42*, 40–47.